Retrieval of Lake Bulk and Skin Temperatures Using Along-Track Scanning Radiometer (ATSR-2) Data: A Case Study Using Lake Tahoe, California

SIMON J. HOOK

Jet Propulsion Laboratory, California Institute of Technology, Pasadena, California

FRED J. PRATA

Atmospheric Research, Commonwealth Scientific and Industrial Research Organization, Aspendale, Victoria, Australia

RONALD E. ALLEY AND ALI ABTAHI

Jet Propulsion Laboratory, California Institute of Technology, Pasadena, California

ROBERT C. RICHARDS

Tahoe Research Group, Department of Environmental Science and Policy, University of California at Davis, Davis, California

S. GEOFFREY SCHLADOW AND SVEINN Ó. PÁLMARSSON

Department of Civil and Environmental Engineering, University of California at Davis, Davis, California

(Manuscript received 23 January 2002, in final form 9 August 2002)

ABSTRACT

In 1999, four monitoring stations were permanently moored on Lake Tahoe, California–Nevada. Each monitoring station provides near-real-time measurements of the surface skin temperature and bulk temperature on a near-continuous basis. Day and night data, acquired over Lake Tahoe from March to August 2000 with the second Along-Track Scanning Radiometer (ATSR-2), have been analyzed, and sets of coefficients for recovering the skin temperature and bulk temperature of the lake have been derived. The field measurements indicate that there is a noticeable difference between the bulk and skin temperatures (skin effect), which varies over the diurnal cycle. At the time of the ATSR-2 daytime overpass, the skin temperatures are on average 0.11°C cooler than the daytime bulk temperatures. At the time of the nighttime ATSR-2 overpass, the skin temperatures are on average 0.46°C cooler than the nighttime bulk temperatures. The smaller skin effect during the day is attributed to strong solar heating and low wind speeds at the site in the morning.

The standard errors for recovering the daytime bulk and nighttime bulk temperatures, by regressing the in situ measurements against the average ATSR-2 nadir 11- and 12-μm channel brightness temperatures, are 0.40° and 0.18°C, respectively. By comparison the standard errors for recovering the daytime skin and nighttime skin temperatures by the same approach are 0.33° and 0.28°C, respectively. The lower standard error obtained for recovery of the skin and bulk temperatures at night is attributed to the lake surface being more homogeneous with the absence of solar heating.

A comparison between the measured skin temperatures, skin temperature recovered by an ATSR-2 two-channel sea surface temperature algorithm, and the in situ regression indicates that the ATSR-2 algorithm has a similar scatter to the in situ linear regression but is offset with respect to the measured skin temperatures.

1. Introduction

The first Along Track Scanning Radiometer (ATSR) (Delderfield et al. 1986) was launched on the *ERS-1* satellite in 1991. Like the Advanced Very High Resolution Radiometer (AVHRR), the ATSR was designed to permit the accurate retrieval of sea surface temperature (SST). The SST measurements derived from ATSR and AVHRR are used for a variety of studies such as global monitoring and understanding large-scale phenomena like El Niño. SST retrievals utilize infrared measurements and both ATSR and AVHRR include three infrared channels located at 3.7, 11, and 12 μm, each having a spatial resolution of about 1 km at nadir. The ATSR differs from the AVHRR in that it includes a dual-view capability and very accurate blackbody sources. The blackbody sources allow calibration of the

Corresponding author address: Dr. Simon J. Hook, Jet Propulsion Laboratory, California Institute of Technology, Pasadena, CA 91109.
E-mail: simon.j.hook@jpl.nasa.gov

radiometer to an accuracy of less than 0.1°C (Mason et al. 1995). These additional features also permit the retrieval of SST from ATSR to an accuracy of 0.3°C (Murray et al. 2000), compared to an accuracy of 0.5°C from AVHRR (McClain et al. 1985), although more recent studies by Kearns et al. (2000) indicate similar results for AVHRR and ATSR.

SST retrievals involve applying a set of coefficients to the data from the infrared channels. These coefficients can be derived by regression of the satellite measurements to a series of in situ buoy temperature measurements (e.g., McClain et al. 1985; Walton et al. 1998) or to a series of modeled SSTs (e.g., Zavody et al. 1995). Both approaches have been validated by in situ measurements (e.g., Schluessel et al. 1987; Barton 1995; Donlon et al. 2002). The two approaches produce different SSTs since the buoy temperature measurements are made at depth, whereas the modeled SSTs utilize the radiometric temperature of the ocean skin. The sea surface skin temperature is typically 0.1°–0.5°C cooler than the bulk temperature, although the difference can vary considerably from this nominal range (Katsaros 1977; Katsaros et al. 1977; Soloviev and Schlussel 1996; Fairall et al. 1996; Wick et al. 1996; Donlon and Robinson 1998; Murray et al. 2000). Both techniques use different coefficients based upon the latitude and climatology of the sea surface under investigation as well as the position of the imaged area within the swath. This dependency on climatology can result in errors in the recovered SST when the climatology differs from the expected range. For example, Donlon and Robinson (1998) report that the dual-view average skin surface temperature algorithm (ASST) of ATSR has a cool −0.54°C bias and that the nadir view ASST has a bias of −0.78°C. The bias is attributed to Saharan dust and aerosols from the Mount Hudson and Mount Pinatubo volcanic eruptions, which were present during the measurement period. This has led to attempts to develop coefficients that correct for the biases (Merchant et al. 1999; Merchant and Harris 1999).

The same approaches developed for deriving coefficients for SST can also be used to develop coefficients for retrieving lake surface temperature. Such maps are valuable for the understanding of a variety of processes in lakes, such as wind-induced upwelling events (Mortimer 1952; Monismith 1985, 1986; Imberger and Patterson 1990) and surface water transport patterns (Strub and Powell 1986, 1987). High-altitude lakes are also useful as validation targets for thermal infrared imaging instruments such as ATSR and AVHRR for two main reasons. First, water bodies typically present a more homogenous surface temperature than land surfaces. Second, since typically there is less water vapor in the atmosphere at higher elevations, the radiation received by the satellite instrument is less perturbed than the radiation from similar sites at lower elevations. For these reasons an automated validation site was established at Lake Tahoe in 1999 for the validation of infrared data from the Advanced Spaceborne Thermal Emission Reflectance Radiometer (ASTER) and Moderate Resolution Imaging Spectroradiometer (MODIS) instruments. Both these instruments are on board the *Terra* spacecraft that was launched into earth orbit in December 1999 (Yamaguchi et al. 1998; Salomonson et al. 1989). The data acquired as part of the ASTER/MODIS validation experiment can also be used to validate other instruments as well as derive coefficients for recovering the lake bulk and skin temperatures. The purpose of this paper is to present a validation dataset for the ATSR-2 satellite instrument that includes both skin and bulk measurements and demonstrate how these data can be used to develop algorithms for recovering the bulk and skin surface temperatures of an inland water body. The ATSR-2 satellite was the replacement for the ATSR satellite that stopped acquiring data in March 2000.

2. Site location and characteristics

Lake Tahoe is a large lake situated in a granite graben near the crest of the Sierra Nevada Mountains on the California–Nevada border, at 39°N, 120°W. The lake level is approximately 1898 m above MSL. The lake is roughly oval in shape with a north–south major axis (33 km long, 18 km wide), and has a surface area of 500 km^2 (Fig. 1). The land portion of the watershed has an area of 800 km^2. Lake Tahoe is considered a deep lake, it is the 11th deepest lake in the world, with an average depth of 330 m, maximum depth of 499 m, and a total volume of 156 km^3. The surface layer of Lake Tahoe deepens during the fall and winter. Complete vertical mixing only occurs every few years. Due to its large thermal mass, Lake Tahoe does not freeze in winter.

3. Field measurements

In order to validate the data from the MODIS and ASTER instruments, the Jet Propulsion Laboratory (JPL) and University of California at Davis (UCD) are currently maintaining four surface sampling stations on Lake Tahoe (Hook et al. 2000). The four stations (rafts) are referred to as TR1, TR2, TR3, and TR4 (Fig. 1). During the period of this study, each raft had a single custom-built self-calibrating Mk I radiometer for measuring the skin temperature and several bulk temperature sensors. The radiometer is mounted on a pole approximately 1 m above the surface of the water that extends beyond the raft (Fig. 2). The radiometer is orientated such that it measures the skin temperature of the water directly beneath it. The radiometer is contained in a single box that is 13 cm wide, 43 cm long, and 23 cm high (Fig. 2). The sensor used in the radiometer is a thermopile detector with a germanium lens embedded in a copper thermal reservoir. The sensor passes radiation with wavelengths between 7.8 and 13.6 μm. The sensor in the Mk I radiometer is mounted in a rotating drum that views the scene and then rotates and views

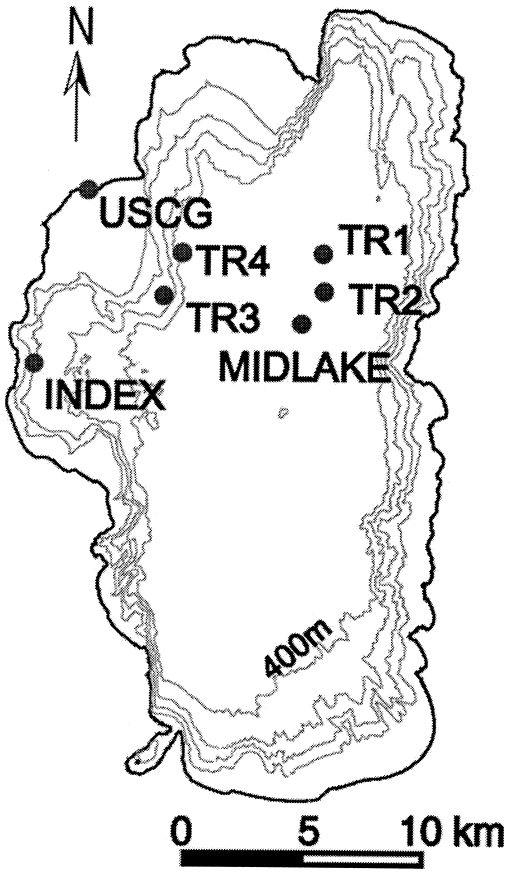

FIG. 1. Bathymetric map of Lake Tahoe with a contour interval of 100 m. The four NASA rafts are labeled TR1, TR2, TR3, and TR4. Also shown are the USCG station and midlake and index stations. A variety of atmospheric measurements are made at the USCG and a variety of water properties are measured at the midlake and index stations.

a hot and cold cone blackbody for calibration. The temperatures of the blackbodies are measured with embedded thermistors. A calibration is performed every 10 min. The unit is completely self-contained and has an onboard computer and memory and operates autonomously. The unit can store data onboard for later download or automatically transmit data to an external datalogger. The unit can be powered for short periods (several hours) with its internal battery or be powered for longer periods with external power. In this study the radiometer was powered externally and data were transferred to an external datalogger. Comparison of the Mk I radiometer against a National Institute of Standards and Technology (NIST) traceable blackbody indicated the radiometer was accurate to ± 0.2 K. NIST traceability is provided by laboratory calibration of the radiometer against the JPL cone blackbody that was traced to NIST using their transfer radiometer (Kanneburg 1998). The Mk I radiometers were replaced with Mk II radiometers in 2001. The Mk II radiometers use a near-nulling blackbody design and have an accuracy of ± 0.1 K. The accuracy of the Mk II radiometers was confirmed in a recent cross-comparison experiment with several other highly accurate radiometers in both a sea trial and in laboratory comparisons (Barton et al. 2002). It should be noted the current design of both the radiometers does not include a sky view and, therefore, the correction for the reflected sky radiation is made using a radiative transfer model (MODTRAN). The correction of the radiometer data is discussed in more detail in section 5.

The bulk water temperature was measured with several temperature sensors mounted on a float tethered behind the raft (Fig. 2). The float was built in the shape of a letter H and was 203 cm long and 70 cm wide. At the end of each point of the letter H was a short leg at

FIG. 2. Surface monitoring station at TR3. The station measures the radiometric skin temperature, bulk temperature, wind direction (magnetic) and speed, relative humidity, air temperature, and net radiation.

right angles to the float and the temperature sensors were attached to the end of the leg approximately 2 cm beneath the surface. Multiple temperature sensors were used to enable cross verification, and each float had up to 12 temperature sensors all at the same depth. The temperature sensors used included Optic Stowaway and Hobo Pro Temperature Loggers available from Onset Corporation (www.onsetcomp.com) and a TempLine system available from Apprise Technologies (www.apprisetech.com). The Optic Stowaway Temperature Loggers include both the sensor and datalogger in a single sealed unit with a manufacturer specified *maximum* error of ± 0.25°C. The Hobo Pro Temp/External Temperature logger has an external temperature sensor at the end of a short cable that returns data to a logger and a manufacturer specified *maximum* error of ± 0.2°C. The TempLine system consists of four temperature sensors embedded at different positions along a cable that is attached to a datalogger. The TempLine system has a manufacturer specified error of ± 0.1°C. Note all sensors are placed at the same depth ensuring both redundancy and cross verification. The calibration accuracy of the Onset temperature sensors was checked using a NIST traceable water bath. NIST traceability was provided by use of a NIST-certified reference thermometer. In all cases the sensors were found to meet the manufacturer specified *typical* error of ± 0.12°C.

Data collected by the external datalogger (radiometer and TempLine system) can be downloaded automatically via cellular telephone. Currently, the external datalogger data are downloaded daily via cellular telephone modem to JPL allowing near-real-time monitoring. A full set of measurements is made every 2 min. However, the units attached to the external datalogger can be remotely reprogrammed if a different sampling interval is desired. A meteorological station (wind speed, wind direction, air temperature, relative humidity, and net radiation) was recently added to TR3 (Fig. 2).

Additional UCD atmospheric deposition collectors are located on TR2 and TR3. Both JPL and UCD maintain additional equipment at the U.S. Coast Guard (USCG) station that provides atmospheric information (Fig. 1). This includes a full meteorological station (wind speed, wind direction, air temperature, relative humidity), full radiation station (long- and shortwave radiation up and down), a shadow band radiometer, and an all-sky camera. The shadow band radiometer provides information on total water vapor and aerosol optical depth. It should be noted the meteorological data may not be representative of conditions on the lake, and for this reason meteorological stations are being added to each raft.

Measurements of algal growth rate using 14°C, nutrients (N, P), chlorophyll, phytoplankton, zooplankton, light, temperature, and secchi disk transparency are also made trimonthly at the index station (Fig. 1) and monthly samples for all constituents except algal growth and light are made at the midlake station (Fig. 1). Many samples are taken annually around the Tahoe Basin to examine stream chemistry and snow and atmospheric deposition constituents.

4. Reduction and analysis of the bulk temperature data

In order to develop algorithms suitable for recovering the bulk and skin temperature of lakes over a wide temperature range, ATSR-2 data acquired between March and August 2000 over Lake Tahoe were evaluated. During this period, the surface temperature of the lake increased from a low of ~ 5°C to a maximum of ~ 22°C. There were 41 ATSR-2 daytime acquisitions over Lake Tahoe during this period. Visual inspection of these data revealed the presence of clouds over or near the lake in 14 of the acquisitions and these were discarded, leaving 27 cloud-free daytime scenes. The ATSR-2 brightness temperatures (BTs) were extracted for the pixel closest to the location of each raft and also the average and standard deviation of the nearest 5×5 pixels. The brightness temperature provided in the ATSR-2 product is the pixel radiance converted to temperature using the Planck function with an assumed emissivity of 1.0. Further details on the ATSR-2 product are available in the ATSR-1/2 user guide (available online at http://www.atsr.rl.ac.uk). Assuming that the ATSR-2 pixel location is accurate to within 1 km, then the recommendation of Minnett (1991) that in situ validation measurements are made within 5 km of a 1-km satellite pixel is met. It should be noted that in certain cases there were shifts in the geolocation information provided with the ATSR-2 data. In all cases the location of validation pixels was checked by visual inspection to make sure they did not include any land pixels and in any cases where the geolocation information was offset, the geolocation information was corrected.

As discussed in the previous section, up to 12 temperature loggers were deployed 2 cm beneath the surface at each raft. Initially the temperature trace of each logger over time was examined to confirm that the logger was reading correctly. This was necessary because the Apprise TempLine and Onset Hobo Pro Temperature logger cables occasionally developed leaks causing the temperature values to drift. The sealed Onset Optic Stowaway Temperature loggers did not drift and were used as a reference to remove any suspect loggers. The calibration of the temperature loggers was also periodically confirmed in a NIST-traceable water bath. For a given logger the two temperature values closest to the overpass time were linearly interpolated to the acquisition time of the nadir pixel. The mean and standard deviation of the interpolated values for each raft were then calculated. Since the interpolation was typically for less than 2 min with a maximum of 5 min, the recommendation by Minnett (1991) that in situ validation measurements

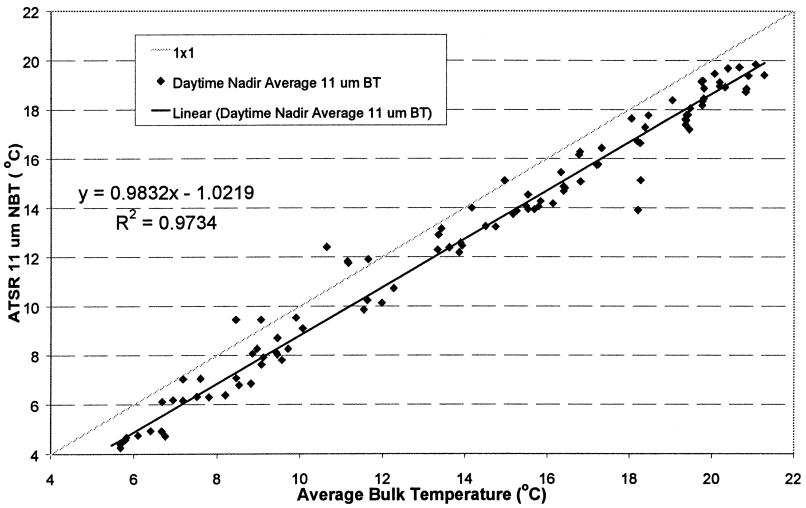

FIG. 3. ATSR-2 visibly cloud-free daytime 5 × 5 average nadir 11-μm BTs over each raft against the average bulk temperature at the time of the overpass.

should be made within ±2 h of the satellite overpass was met.

Figures 3 and 4 show plots of the daytime nadir 5 × 5 average 11- and 12-μm BTs for the 27 cloud-free overpasses plotted against the average bulk temperatures for each raft. Examination of these plots indicates that the deviation of the average nadir BTs from the average bulk temperatures is less for the 11-μm than the 12-μm average nadir BTs. Also, the correlation of the 11-μm average nadir BTs to the average bulk temperatures is better than the corresponding correlation for the 12-μm BTs. Both of these effects are expected since the average nadir BTs are more strongly influenced by the atmosphere at 12 than 11 μm.

Standard deviations of the bulk temperature measurements at the time of each overpass for the measurement period (March–August 2000) are shown in Fig. 5. Figure 6 shows the standard deviations of the average nadir 11-μm BTs at corresponding overpass times. Examination of these plots indicates there were several occasions when there was some heterogeneity in both the ATSR-2 brightness temperatures and in situ bulk temperatures, and there is some seasonal dependence to the variation in standard deviations with greater variation in the spring and early summer. Also the standard deviations of TR1, TR2, and TR3 are generally lower than those of TR4. The lower standard deviations of TR1, TR2, and TR3 are thought to be due to two processes. First, TR3 and TR4 are in shallower water than TR1 and TR2 (see Fig. 1) and therefore more likely to be influenced by any internal waves (Rueda et al. 2002). Second, TR4 is adjacent to a large shallow shelf

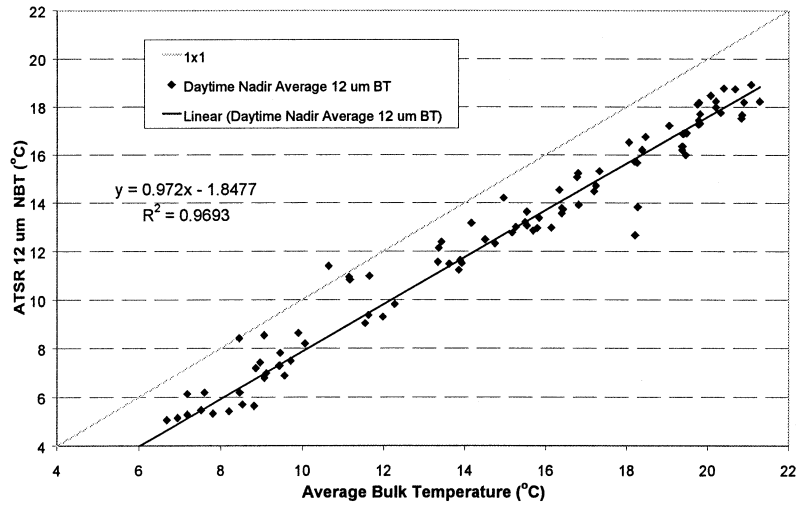

FIG. 4. ATSR-2 visibly cloud-free daytime 5 × 5 average nadir 12-μm BTs over each raft against the average bulk temperature at the time of the overpass.

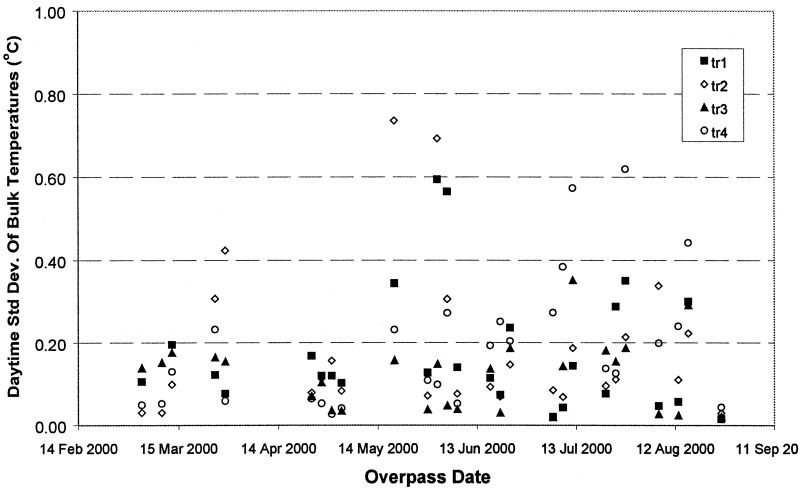

FIG. 5. Std dev of the bulk temperature measurements at the time of each overpass from each raft for the measurement period (Mar–Aug 2000).

to the west of the raft, and since the prevailing winds are from the southwest, any warm water that develops over the shelf will be pushed past TR4, which could result in a larger standard deviation. The generally larger standard deviation of the measurements made in spring to early summer results from more frequent calm days with strong solar heating during this period.

Figure 7 shows a plot of the difference between the daytime average nadir 11- and 12-μm BTs against the total water vapor (TWV) available from the National Centers for Environmental Prediction (NCEP). NCEP produces global model values on a $1° \times 1°$ grid at 6-h intervals. Lake Tahoe is centered on 39°N, 120°W and the grid value for this point was utilized. The NCEP data were not interpolated to the overpass time. However, this was typically within 2 h of the daytime overpass. Examination of this plot indicates that the TWV is not strongly correlated with the difference between the 11- and 12-μm average nadir BTs. This lack of correlation is attributed to the small amounts of water vapor (total column water = 0.5–1.5 cm) present in the atmosphere over Lake Tahoe during the ATSR-2 overpasses utilized for this study.

While these data could be used in a regression to obtain the coefficients for recovering the bulk temperature of the lake, the dataset includes scenes in which the standard deviation of the ATSR-2 and field data are larger than would be expected under ideal conditions. These higher standard deviations can be attributed to real variations in the lake skin temperature as well as possible cloud contamination from subvisible cirrus. Since an objective of this study is to produce algorithms for recovering the bulk and skin temperatures, it was decided to remove any points where real surface het-

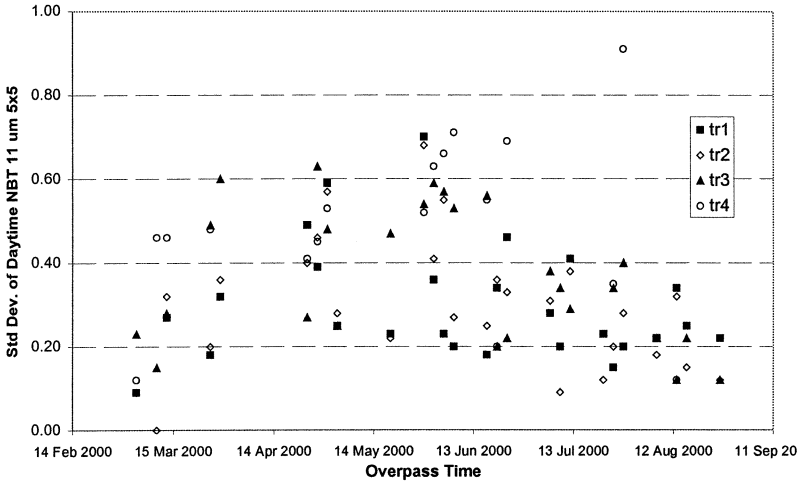

FIG. 6. Std dev of the ATSR-2 visibly cloud-free daytime 5×5 average nadir 11-μm BTs over each raft for the measurement period (Mar–Aug 2000).

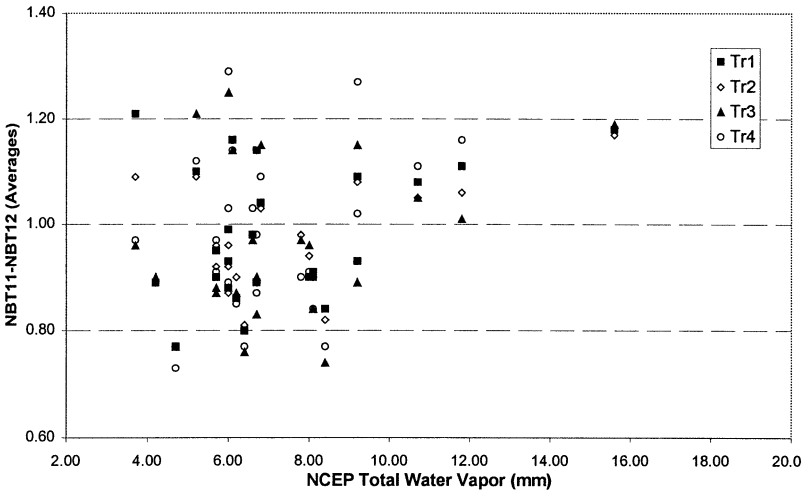

FIG. 7. Difference between the ATSR-2 visibly cloud-free daytime average nadir 11- and 12-μm BTs against the total water vapor available from NCEP.

erogeneity may be causing a poor match between the field and satellite values. In order to remove the values with large standard deviations, any points with a standard deviation of greater than 0.3°C in either the field measurements or ATSR-2 average nadir BTs were removed. Figure 8 shows a plot of the data shown in Fig. 3 with any values with a standard deviation in either the field or ATSR-2 5 $\times$ 5 average nadir BTs for the 11- and 12-μm bands removed. (The numerical values for these points are available by request from the first author.) Clearly, this results in far less scatter in the data and an improved correlation coefficient ($r^2 = 0.9945$). Originally there were 107 values in the dataset. After removing any values in which the standard deviation of the image data was greater than 0.3°C, the dataset was reduced to 45 values. The 45 values were further reduced to 38 values by removing any values in which the standard deviation of the bulk temperature data was greater than 0.3°C. This reduced dataset is henceforth referred to as the filtered daytime dataset. The number of samples from TR4 in the filtered daytime dataset was dramatically reduced compared to those from the other three rafts as expected if the water surrounding the raft was influenced by the water from the nearby shelf. It is important to recognize that the objective of this work is to develop an algorithm for recovering the bulk and skin temperatures from ATSR-2 data and therefore the optimum dates for matching the field data with the satellite data were selected using the 0.3°C criterion.

Standard deviations of the bulk temperature values

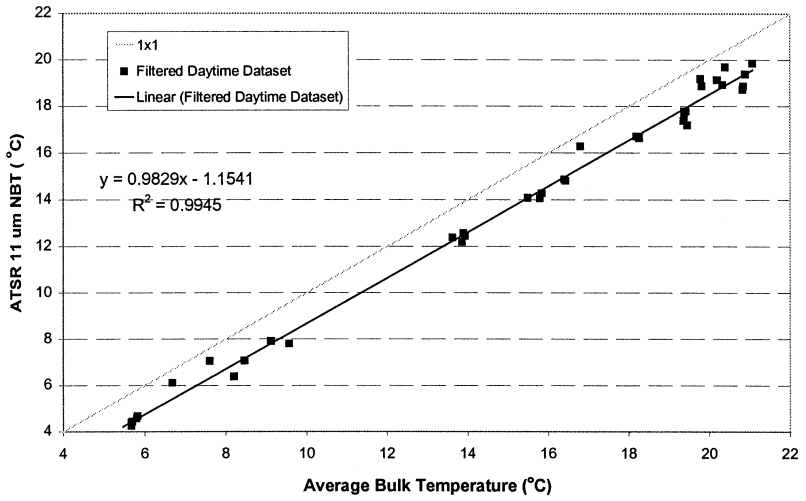

FIG. 8. Visibly cloud-free daytime average nadir 11-μm BTs from each raft vs the average bulk temperatures at each raft at the time of the ATSR-2 overpass after removing any values with a std dev in the field or ATSR-2 data greater than 0.3 (filtered daytime dataset).

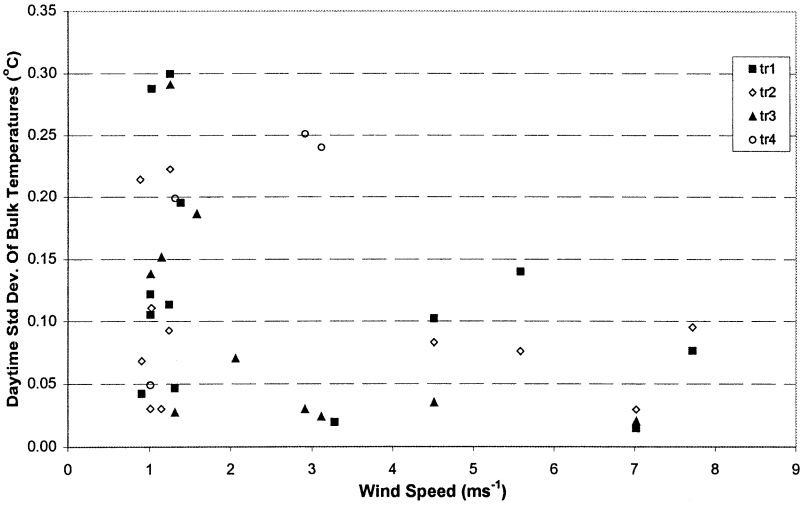

FIG. 9. Std dev of the bulk temperatures vs the wind speed measured at the USCG station (Fig. 1) for the filtered daytime dataset.

versus wind speed measured at the U.S. Coast Guard station for the filtered daytime dataset are shown in Fig. 9. Clearly, higher standard deviations are associated with lower wind speeds. This relationship is due to the top few centimeters of the lake warming unevenly on clear calm days as opposed to clear windy days when the top few centimeters are well mixed (Katsaros 1977; Katsaros et al. 1997; Soloviev and Schlussel 1996; Fairall et al. 1996; Wick et al. 1996; Donlon and Robinson 1998; Murray et al. 2000).

In addition to the daytime dataset, a similar sized nighttime dataset was also acquired. The nighttime dataset included 144 observations. Figure 10 shows a plot of the standard deviations of the bulk temperature values for the 144 measurements at the time of the nighttime overpasses. The lack of any solar influence clearly affects the standard deviations of the field data with all the values, except for two outliers, having standard deviations of less than 0.15°C. Figure 11 shows the standard deviations of the bulk temperature values plotted against wind speed. It is apparent that the majority of values cluster around wind speeds of 1–3.5 m s^{-1} and the standard deviation is no longer greater for lower wind speeds as seen during the day. The lower standard deviations are thought to result from the surface being well mixed by higher winds in the late afternoon and early evening and continuing to be convectively mixed throughout the night due to the stronger buoyancy flux.

Since cloudy scenes were difficult to remove by inspection of the nighttime data, the nadir BTs from the 11- and 12-μm channels were filtered using the same criteria as outlined for the daytime data (any values with

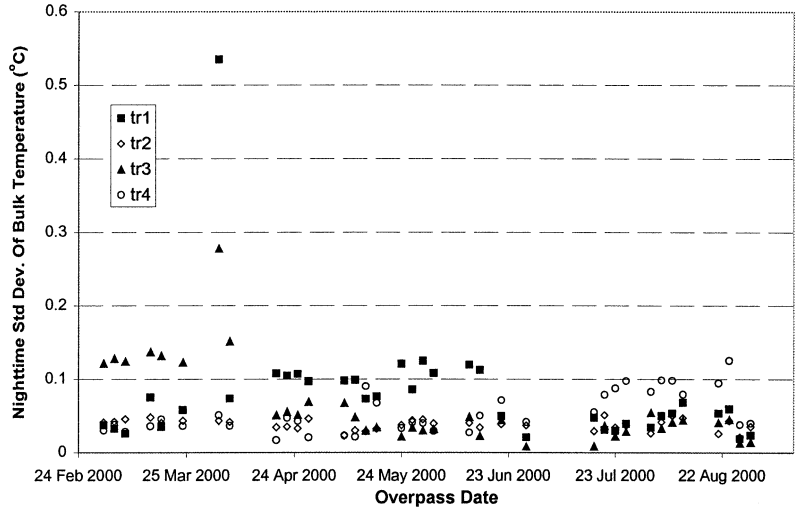

FIG. 10. Std dev of the nighttime bulk temperatures at the time of the ATSR-2 overpasses.

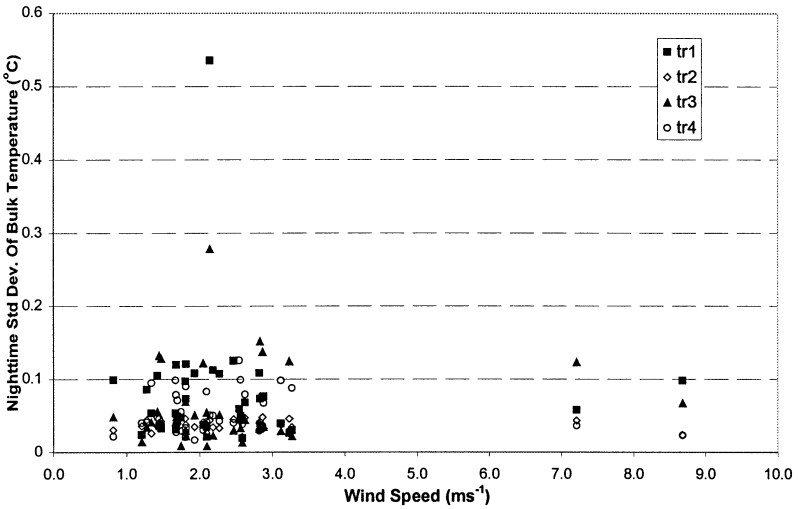

FIG. 11. Std dev of the nighttime bulk temperatures at the time of the ATSR-2 overpasses vs the wind speed measured at the USCG station (Fig. 1).

a standard deviation greater than 0.3°C in the bulk or ATSR-2 nadir 11- and 12-μm average BTs were removed). Filtering of the ATSR-2 values reduced the number of values from 144 to 52. One further value was removed in which the standard deviation of the field data was greater than 0.3°C, resulting in a filtered nighttime dataset consisting of 51 values (Fig. 12). (The numerical values for these points are also available by request from the first author.) After filtering, the number of values selected from each of the four rafts was approximately the same. This contrasts with the daytime measurements, where the water temperature around TR4 had a larger standard deviation than around the other rafts, and supports the suggestion that during the day the water around TR4 is influenced by water from the adjacent shelf. The correlation coefficient, after filtering, is similar to the daytime dataset ($r^2 = 0.9961$).

5. Reduction and analysis of the skin (radiometric) temperature data

The skin temperatures for the filtered daytime and nighttime datasets were calculated from the radiometer data. In order to obtain the skin (kinetic) temperature, it is necessary to correct the data for any atmospheric and emissivity effects (Hook et al. 2000). The skin temperature is derived by correcting for surface emissivity and subtracting the sky radiance reflected by the surface into the path of the radiometer:

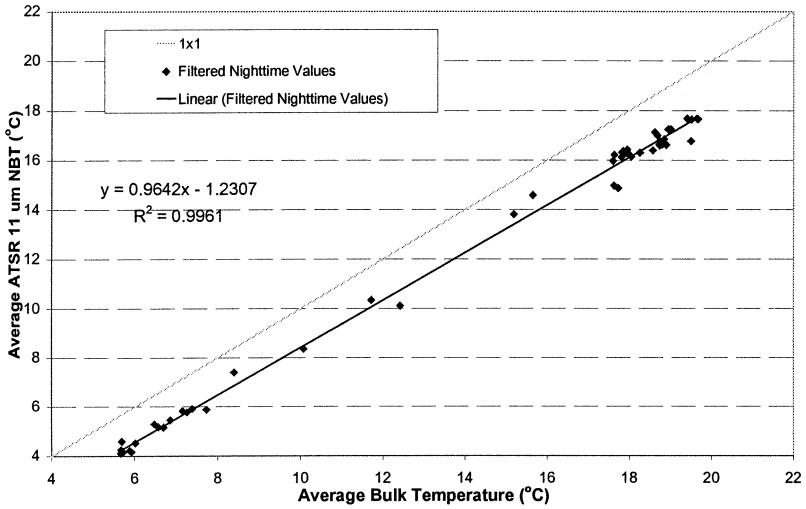

FIG. 12. ATSR nighttime average nadir 11-μm BTs from each raft vs the average bulk temperatures at each raft at the time of the ATSR-2 overpass after removing any values with a std dev in the field or ATSR-2 data greater than 0.3 (filtered nighttime dataset).

$$L_{\text{obs}} = \int_{\lambda} R(\lambda)\left\{L_{\text{path}}(\lambda) + \tau(\lambda)\varepsilon(\lambda)L_{\text{BB}}(T, \lambda) + \tau(\lambda)[1 - \varepsilon(\lambda)]\frac{I_{\text{sky}}(\lambda)}{\pi}\right\} d\lambda, \quad (1)$$

where L_{obs} is the observed radiance at sensor, R is the normalized system spectral response function, λ is the wavelength, L_{path} is the emitted radiance from surface–sensor path, τ is the surface–sensor path transmittance, ε is the surface emissivity, L_{BB} is the blackbody radiance (Planck function), T is the temperature, and I_{sky} is the total downwelling irradiance upon the surface.The path transmittance, path radiance, and downwelling irradiance terms are obtained from a radiative transfer model (MODTRAN 3.5) driven by a supplied atmospheric profile. The NCEP profiles described earlier were used as inputs to the radiative transfer model and were interpolated to the overpass time. With all terms of (1) determined, the equation was solved for temperature by iteration. The radiative transfer model was run at full resolution (1 wavenumber) and the result convolved to the ATSR-2 system response function. Since the radiometer is 1 m above the surface and views the surface in the nadir position (down looking), the surface transmittance and path radiance terms are essentially 1 and 0, respectively. They are included for completeness.

The emissivity of water was obtained from the ASTER spectral library (available online at speclib.jpl.nasa.gov). Shipborne radiometers typically view the surface at an angle up to 55° (e.g., Barton et al. 2002). Errors in the knowledge of the surface emissivity can result in large errors in the corrected temperature. The possibility of such errors is far greater for instruments that view the surface off-nadir since the emissivity of water decreases and exhibits a greater range with increasing view angle. When viewed off-nadir, the emissivity of water is also more strongly affected by wind speed (Wu and Smith 1997).

In order to assess the effect of using modeled data rather than a direct sky view to correct the data for reflected downwelling sky radiation, a sensitivity analysis was performed. For the sensitivity analysis cold and hot brightness temperatures were assumed to have been measured by the radiometer and the surface kinetic temperature derived using a water emissivity spectrum and standard atmospheric profile. The water emissivity spectrum was obtained from the ASTER spectral library; the U.S. Standard Atmospheric profile included with MODTRAN (Berk et al. 1989) was used as the standard atmospheric profile. The results of the sensitivity analysis are shown in Table 1. The initial brightness temperatures measured by the radiometer were 5.0° and 20.0°C, which after emissivity and downwelling sky correction mapped to 5.579° and 20.703°C, respectively. If no sky correction was necessary, the corrected values would be 5.779° and 20.871°C, respectively. Sky correction reduces the difference between the measured and corrected values by 0.200° and 0.168°C. In order to assess the effects of any errors in the input profile on the downwelling sky correction, the atmospheric profile was adjusted, the correction recalculated, and the difference between the original and adjusted kinetic temperature calculated. The water vapor profile was adjusted by 30%, the temperature profile was adjusted by 2°C, and the ozone profile adjusted by 50%. Examination of the results indicates that the largest difference caused by an assumed error in the profile was due to water vapor and this was 0.018°C, well below the accuracy of the radiometers.

TABLE 1. Sensitivity analysis of the effect of errors in the atmospheric profile on the correction for reflected downwelling radiation from the radiometer data.

Perturbation	Kinetic temp (°C)		Diff from no perturbation	
None	5.579	20.703	0.000	0.000
No sky radiance	5.779	20.871	0.200	0.168
Water factor 0.7	5.596	20.715	0.017	0.012
Water factor 1.3	5.561	20.691	−0.018	−0.012
Air temp −2.0°C	5.590	20.712	0.011	0.009
Air temp +2.0°C	5.568	20.694	−0.011	−0.009
Ozone factor 0.5	5.585	20.709	0.006	0.006
Ozone factor 1.5	5.574	20.700	−0.005	−0.003

In certain cases in the filtered daytime and nighttime datasets, a matching set of radiometer data was not recorded with the bulk temperature data for a particular raft for an overpass. If no radiometer data were available for a raft on a given day in the filtered datasets, but data were available from other rafts for that day, then the average of the skin effect (difference between the bulk and skin temperatures) from the other rafts was used with the average bulk temperature data that were available for the raft to calculate a skin temperature. If no radiometer data were available for that day in the filtered dataset, then the overall average of the skin effect for all recording radiometers in the filtered dataset was used, with the bulk temperature for that day to obtain the skin temperature. (A complete set of bulk and skin temperatures for the rafts at the time of the overpass is available by request from the first author.) The average skin effect of all the directly measured daytime values is 0.11°C, compared to 0.46°C for the nighttime values. The smaller skin effects observed in the daytime values are attributed primarily to strong solar heating coupled with low wind speeds resulting in greater stratification. Figure 13 shows a plot of field data acquired over Lake Tahoe at the TR3 station on 7 June 2001. These data were derived using the Mk II radiometer and include simultaneous meteorological data. Notice that as the solar elevation increases, the bulk and skin temperatures both increase, with the skin temperature increasing more rapidly and surpassing the bulk temperature until the early afternoon. In the early afternoon the wind increases, resulting in a reduction in the skin and bulk tem-

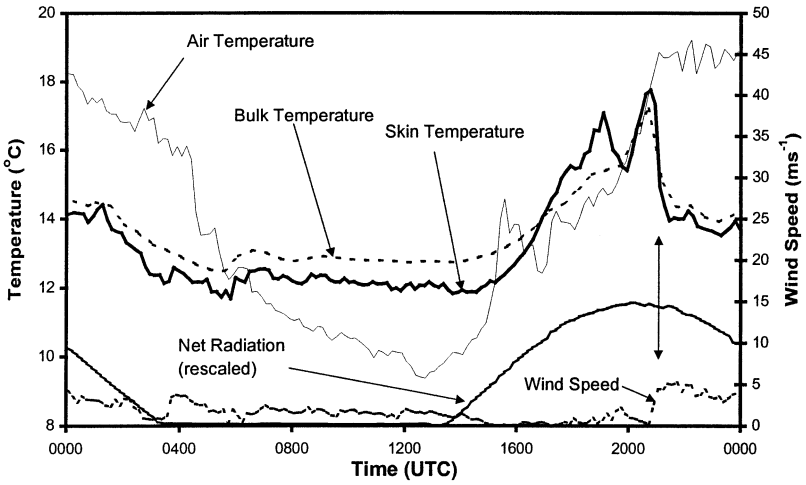

FIG. 13. Variations in the bulk, skin, air temperatures and wind speed on 7 Jun 2001 at Lake Tahoe. The lake begins warming around 6 A.M. (1400 UTC) and increases steadily from a minimum of 12°C to a maximum of 17.4°C. During the warming period, the skin (measured by the radiometer) warms more rapidly than the bulk and can exceed the bulk temperature. At 1 P.M. (2100 UTC) wind speed increases (marked by double arrow), as is typical, with warm air from the land blowing over the lake. This causes a rapid decrease in temperature due to mixing of cooler water at depth with the heated skin. By the early evening a well-developed skin has been established that persists until the following morning. Bulk temperature (dashed line), skin temperature (heavy solid line), air temperature (solid line), wind speed (dashed line), net radiation (solid line). Note net radiation was rescaled to enable display on plot.

peratures (shown by a double arrow on Fig. 13). The morning increase in the bulk temperatures is also associated with an increase in the standard deviation of the bulk temperature measurements (not shown). The standard deviation of the bulk temperatures also decreases in the early afternoon as the wind increases due to greater mixing. In the late afternoon, the wind speed decreases and a skin/bulk differential is established that remains fairly constant throughout the night. As the wind speed increases in the early afternoon, so does the air temperature as warm air from the adjacent land is blown over the lake. Days characterized by low wind speeds and strong solar heating occur predominantly in the spring and early summer. Inspection of the filtered daytime values reveals that data from the spring and early summer are preferentially filtered out with the criteria that the standard deviation of the bulk temperature data must be less than 0.3°C. The standard deviation of the daytime skin effect, using the directly measured values, is greater (0.43°C) than the standard deviation of the nighttime skin effect (0.21°C) using the directly measured skin values. The higher standard deviation of the daytime skin effect is attributed to the greater and more variable stratification during the day due to the lower wind speeds and higher solar irradiance. These data suggest that nighttime overpasses are more suitable for validation if only bulk temperature data are available and a constant skin effect must be assumed, although this makes cloud filtering more difficult. Recent work by Donlon (1999) suggests that the assumption of a constant skin effect may be more appropriate if wind speeds are greater than 6 m s^{-1}, regardless of day or night.

Figure 14 is a plot of the skin temperature versus the 11-μm channel average brightness temperature for the filtered daytime dataset. Figure 15 is the equivalent plot for the filtered nighttime data. The scatter of the fit line is similar for both the daytime and nighttime since the skin measurement is measuring the same surface as the satellite radiometer.

6. Regression coefficients

Table 2 provides the coefficients from multiple linear regressions of the average nadir 11- and 12-μm channel brightness temperatures against the various in situ datasets. Table 2 also includes the r^2 values and standard error of the fit for each regression (Triola 1983). Examination of these data indicates that the standard errors for the regression of the ATSR-2 data against the daytime bulk and skin temperature data are greater than those for the corresponding nighttime data. The smaller error for the nighttime datasets is attributed to the lake surface being more homogenous at night with the absence of solar heating. Solar heating induces local variation in the skin and bulk temperatures as indicated by the larger standard deviations of the bulk temperature data at the ATSR-2 daytime overpass time as compared to the nighttime overpass time. The standard error of the ATSR-2 data to the daytime bulk data is slightly

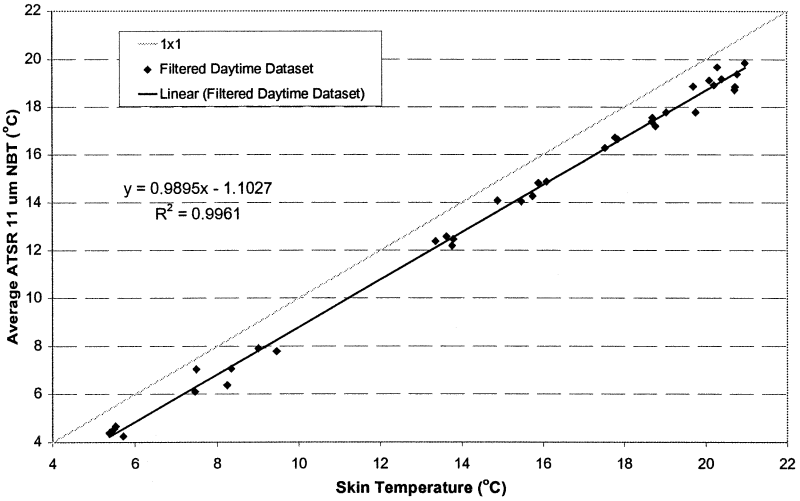

FIG. 14. Daytime average nadir 11-μm BTs from each raft vs the skin temperature at each raft at the time of the ATSR-2 overpass, after removing any values with a std dev in the field or ATSR-2 data greater than 0.3 (filtered daytime dataset).

worse than the standard error of the daytime skin data. This suggests that the satellite data can provide a better estimate of the skin temperature than the bulk temperature, presumably since the bulk data will always include additional scatter caused by the skin effect. The standard error of the nighttime bulk temperature retrievals is slightly better than the skin temperature retrievals. This result is surprising and most likely due to the greater accuracy of the bulk temperature sensors compared to the Mk I radiometer. The standard errors for the regression of the satellite data to the bulk and skin temperature datasets are similar and within the ranges observed for oceans datasets (McClain et al. 1985; Murray et al. 2000).

7. Comparison to an ATSR-2 two-channel SST algorithm

The average nadir brightness temperatures for the 11- and 12-μm channels were also used to calculate the surface skin temperature using an ATSR-2 two-channel SST algorithm with coefficients derived by C. Merchant and transmitted to the authors by J. Murray (2002, personal communication). The algorithm calculates two SSTs: one for nadir and the other as if the sensor were viewing at the extreme edge of the scan. These two values are then interpolated using the pixel number to give the SST at the view pixel.

The algorithms are

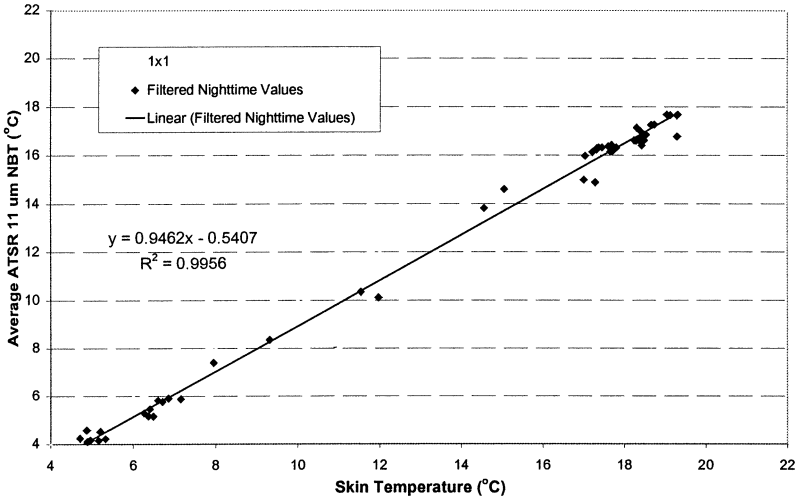

FIG. 15. Nighttime average nadir 11-μm BTs from each raft vs the skin temperature at each raft at the time of the ATSR-2 overpass, after removing any values with a std dev in the field or ATSR-2 data greater than 0.3 (filtered nighttime dataset).

TABLE 2. Linear coefficients derived from a multiple linear regression of the average nadir 11- and 12-μm ATSR-2 BTs against the average bulk temperature values for the four Tahoe rafts at the time of the ATSR-2 overpass.

Coeff used	Intercept	X1	X2	N	r^2	Std error
Daytime bulk	−0.0162	2.5456	−1.5538	38	0.9953	0.3984
Nighttime bulk	0.1788	2.5680	−1.5645	51	0.9990	0.1784
Day and night bulk	0.1201	2.5659	−1.5703	89	0.9965	0.3393
Daytime skin	−0.0005	2.4225	−1.4344	38	0.9968	0.3276
Nighttime skin	−0.3658	2.3823	−1.3556	51	0.9977	0.2786
Day and night skin	−0.2384	2.4392	−1.4306	89	0.9970	0.3132

$$\text{nad\_sst} = a_0 + a_1 t_{12n} + a_2 t_{11n}$$

$$\text{edg\_sst} = b_0 + b_1 t_{12n} + b_2 t_{11n}$$

$$\text{sst} = \text{nad\_sst} + (\text{edg\_sst} - \text{nad\_sst})\left(\frac{\text{air\_mass}(i) - 1}{0.07651}\right),$$

where nad_sst = nadir sea surface temperature (K), edg_ss = edge sea surface temperature (K), sst = sea surface temperature (K), t_{12n} = 12-μm nadir brightness temperature (K), t_{11n} = 11-μm nadir brightness temperature (K), i = pixel number (0 − 511), a_0 = −1.30000, a_1 = −2.68950, a_2 = +3.69181, b_0 = −1.54000, b_1 = −2.77260, and b_2 = +3.77560. The air_mass is the airmass factor calculated for 256 values (symmetric about the nadir direction) according to the viewing geometry.

Figure 16 shows the skin temperatures recovered from the ATSR-2 data using the two-channel SST algorithm and the in situ linear regression against the measured skin temperatures. Table 3 gives the mean difference, standard deviation, and standard error of the mean between the recovered skin temperatures using the ATSR-2 algorithm and the measured skin temperatures for the daytime and nighttime filtered data. Examination of Fig. 16 and Table 3 indicates that the ATSR-2 SST algorithm overestimates skin temperature and that the scatter of the recovered to measured values is similar to using the in situ regression algorithm. This result indicates you cannot simply take the ATSR-2 SST algorithm and apply it to land-locked lakes. The reasons the ATSR-2 SST algorithm does not work well at Lake Tahoe are probably multifold and include both atmospheric and surface effects (e.g., aerosols, water vapor, salinity). These same reasons may also mean that the in situ regression will not work well at other lakes, but further work is required to determine whether this is the case and also to understand any implications for the ATSR-2 algorithm.

8. Summary and conclusions

In 1999, four monitoring stations were permanently moored on Lake Tahoe, California–Nevada. Each monitoring station provides measurements of the surface skin and bulk temperature every 2 min on a continuous basis. These data were used to develop algorithms to recover the bulk and skin temperature of the lake using data from the ATSR-2. This involved comparing ATSR-2 data acquired between March and August 2000 over Lake Tahoe with the corresponding ground measurements. Initially, the average ATSR-2 nadir brightness

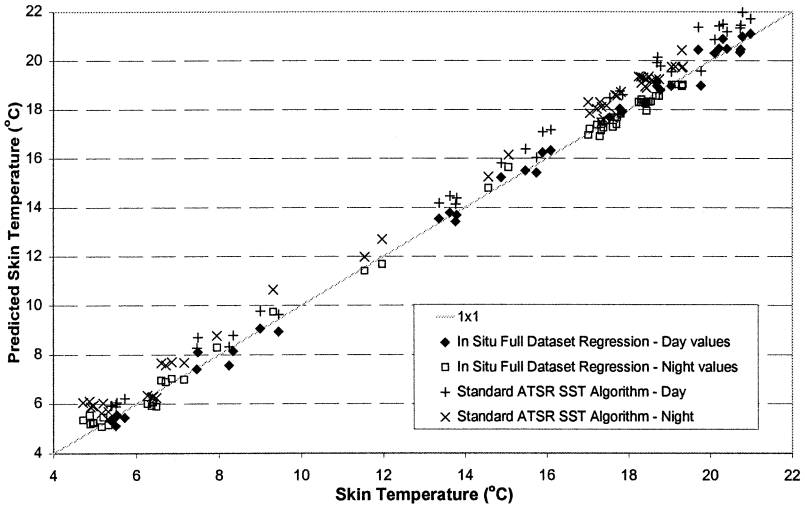

FIG. 16. Predicted skin temperature from the ATSR-2 values using the ATSR-2 SST algorithm and in situ datasets against the skin temperatures.

TABLE 3. Mean and std dev of the difference between the surface skin temperature derived using the standard ATSR-2 SST algorithm and the measured skin temperature.

Dataset	Mean diff (ATSR-in situ °C)	Std dev of diff (ATSR-in situ °C)	Std error of mean diff
Daytime	0.76	0.39	0.0628
Nighttime	0.69	0.38	0.0533

temperatures from the 11- and 12-μm channels for 5 $\times$ 5 pixels centered on each of the rafts from the cloud-free daytime overpasses were plotted against the corresponding bulk temperatures. As expected, the plots showed a strong correlation between the satellite data and ground measurements ($r^2 = 0.9734$, 11-μm channel). In order to reduce the scatter, the dataset was filtered by excluding any points in which the standard deviation of the 5 $\times$ 5 pixels, centered on each raft in the 11- and 12-μm channels, and corresponding standard deviation of the bulk temperature values were greater than 0.3°C. Filtering reduced the daytime dataset from 107 points to 38, increased the r^2 value to 0.9945 (11-μm channel) and reduced the scatter. A similar filter was applied to the nighttime data that reduced the dataset from 144 to 51 points with an r^2 value of 0.9961. The scatter was attributed to real variations in the surface temperature due to differential solar heating and was especially prevalent on days with strong diurnal cycles in the spring and early summer associated with low wind speeds and clear weather.

The ATSR-2 11- and 12-μm channel values were then regressed against the corresponding ground measurements in the filtered dataset to obtain sets of coefficients for recovering the bulk and skin temperatures. Separate coefficients were derived for recovering the daytime skin, daytime bulk, nighttime skin, nighttime bulk, day and night skin, and day and night bulk temperatures. Evaluation of the standard errors indicated that the smallest errors were obtained using the nighttime datasets. This result was attributed to the temperature of the lake being more homogenous at night when it was not subjected to differential solar heating.

The ATSR-2 sea surface temperature algorithm was also applied to the data and the recovered skin temperatures were compared to the measured skin temperatures. The algorithm overestimated the measured skin temperature but had a similar scatter to the in situ algorithms.

The results confirm that a similar skin effect to that observed over the oceans is observed over lakes and that skin effect is of a similar magnitude to that seen over the oceans. The results also indicate that solar heating on calm days can result in considerable variation in the size of the skin effect.

To date, few studies have attempted to use surface temperatures derived from satellite data for lake studies compared to ocean studies, in part, due to the lack of suitable algorithms. This study provides an algorithm for recovering the surface temperature of lakes in areas where the total atmospheric water is low. Future work will focus on utilizing the validation data acquired at Lake Tahoe to validate data from other satellite radiometers as well as develop algorithms for retrieving surface temperatures from data acquired by other satellite radiometers for limnological studies.

Acknowledgments. The research described in this paper was carried out in part at the Jet Propulsion Laboratory, California Institute of Technology, under a contract with the National Aeronautics and Space Administration as part of the Earth Observing System Mission to Planet Earth Program.

Numerous people have contributed to this work. In particular we would like to thank Serj Zadourian and Tim Thompson from JPL. The UCD Tahoe Research Group is also thanked for providing numerous suggestions and information in general on Lake Tahoe.

The ATSR data were acquired by the ESA and processed courtesy of RAL. Joe Murray is thanked for supplying the ATSR SST algorithm coefficients.

Reference herein to any specific commercial product, process, or service by trade names, trademark, manufacturer, or otherwise does not imply endorsement by the United States or the Jet Propulsion Laboratory, California Institute of Technology.

REFERENCES

Barton, I. J., 1995: Satellite-derived sea-surface temperatures—Current status. *J. Geophys. Res.,* **100C,** 8777–8790.

Berk, A., L. S. Bernstein, and D. C. Robertson, 1989: MODTRAN: A moderate resolution model for LOWTRAN 7. Tech. Rep. GL-TR-89-0122, Airforce Geophysical Laboratory, Bedford, MA, 38 pp.

Delderfield, J., D. T. Llewellyn-Jones, R. Bernard, Y. de Javel, E. J. Williamson, I. Mason, D. R. Pick, and I. J. Barton, 1986: The Along Track Scanning Radiometer (ATSR) for *ERS-1. Proc. SPIE,* **589,** 114–120.

Donlon, C. J., 1999: Implications of the oceanic SST deviation at high wind speed. *Geophys. Res. Lett.,* **26,** 2505–2508.

——, and I. S. Robinson, 1998: Radiometric validation of *ERS-1* Along Track Scanning Radiometer average sea surface temperature in the Atlantic Ocean. *J. Atmos. Oceanic Technol.,* **15,** 647–660.

——, P. J. Minnett, C. Gentemann, T. J. Nightingale, I. J. Barton, B. Ward, and M. J. Murray, 2002: Toward improved validation of satellite sea surface skin temperature measurements for climate research. *J. Climate,* **15,** 353–369.

Fairall, C. W., E. F. Bradley, J. S. Godfrey, G. A. Wick, J. B. Edson, and G. S. Young, 1996: Cool-skin and warm-layer effects on sea surface temperature. *J. Geophys. Res.,* **101C,** 1295–1308.

Hook, S. J., A. R. Prata, and S. G. Schladow, cited 2000: Interim status report. [Available online at http://eospso.gsfc.nasa.gov/validation/terraval.html.]

Imberger, J., and J. C. Patterson, 1990: Physical limnology. *Adv. Appl. Mech.,* **27,** 303–475.

Kannenberg, B., 1998: IR instrument comparison workshop at the Rosenstiel School of Marine and Atmospheric Science (RSMAS). *The Earth Observer,* Vol. 10, No. 3, 51–54.

Katsaros, K. B., 1977: Sea-surface temperature deviation at very low wind speeds—Is there a limit? *Tellus,* **29,** 229–239.

——, W. T. Liu, J. A. Businger, and J. E. Tillman, 1977: Heat-trans-

port and thermal structure in interfacial boundary-layer measured in an open tank of water in turbulent free convection. *J. Fluid Mech.,* **83,** 311.

Kearns, E. J., J. A. Hanafin, R. H. Evans, P. J. Minnett, and O. B. Brown, 2000: An independent assessment of pathfinder AVHRR sea surface temperature accuracy using the Marine Atmosphere Emitted Radiance Interferometer (MAERI). *Bull. Amer. Meteor. Soc.,* **81,** 1525–1536.

Mason, I. M., P. H. Sheather, J. A. Bowles, and G. Davies, 1995: Black body calibration sources of high accuracy for a spaceborne infrared instrument, the along track scanning radiometer. *Appl. Opt.,* **35,** 629–639.

McClain, E. P., W. G. Pichel, and C. C. Walton, 1985: Comparitive performance of AVHRR multichannel SSTs. *J. Geophys. Res.,* **90,** 11 587–11 601.

Merchant, C. J., and A. R. Harris, 1999: Toward the elimination of bias in satellite retrievals of sea surface temperature. 2. Comparison with in situ measurements. *J. Geophys. Res.,* **104,** 23 579–23 590.

——, ——, M. J. Murray, and A. M. Zavody, 1999: Toward the elimination of bias in satellite retrievals of sea surface temperature. *J. Geophys. Res.,* **104,** 23 565–23 578.

Minnett, P. J., 1991: Consequences of sea surface temperature variability on the validation and application of satellite measurements. *J. Geophys. Res.,* **96,** 18 475–18 489.

Monismith, S. G., 1985: Wind-forces motion in stratified lakes and their effect on mixed-layer shear. *Limnol. Oceanogr.,* **30,** 771–783.

——, 1986: An experimental study of the upwelling response of stratified reservoirs to surface shear stress. *J. Fluid Mech.,* **171,** 407–439.

Mortimer, C. H., 1952: Water movements in lakes during summer stratification: Evidence from the distribution of temperature in Windermere. *Philos. Trans. Roy. Soc. London,* **B236,** 355–404.

Murray, M. J., M. R. Allen, C. J. Merchant, A. R. Harris, and C. J. Donlon, 2000: Direct observation of the skin-bulk SST variability. *Geophys. Res. Lett.,* **27,** 1171–1174.

Rueda, F. J., S. G. Schladow, and S. O. Palmarsson, 2002: Basin-scale internal wave dynamics during a winter cooling period in a large lake. *J. Geophys. Res.,* in press.

Salomonson, V. V., W. L. Barnes, P. W. Maymon, H. E. Montgomery, and H. Ostrow, 1989: MODIS: Advanced facility instrument for studies of the earth as a system. *IEEE Trans. Geosci. Remote Sens.,* **27,** 145–153.

Schluessel, P., H. Y. Shin, W. J. Emery, and H. Grassl, 1987: Comparison of satellite-derived sea-surface temperatures with in situ skin measurements. *J. Geophys. Res.,* **92C,** 2859–2874.

Soloviev, A. V., and P. Schlussel, 1996: Evolution of cool skin and direct air–sea gas transfer coefficient during daytime. *Bound.-Layer Meteor.,* **77,** 45–68.

Strub, P. T., and T. M. Powell, 1986: Wind-driven surface transport in stratified closed basins: Direct versus residual calculation. *J. Geophys. Res.,* **91,** 8497–8508.

——, and ——, 1987: Surface temperature and transport in Lake Tahoe: Inferences from satellite (AVHRR) imagery. *Contin. Shelf Res.,* **7,** 1001–1013.

Triola, M. F., 1983: *Elementary Statistics.* Benjamin/Cummings, 496 pp.

Walton, C. C., W. G. Pichel, J. F. Sapper, and D. A. May, 1998: The development and operational application of nonlinear algorithms for the measurement of sea surface temperatures with the NOAA polar-orbiting environmental satellites. *J. Geophys. Res.,* **103C,** 27 999–28 012.

Wick, G. A., W. J. Emery, L. H. Kantha, and P. Schlussel, 1996: The behavior of the bulk-skin sea surface temperature difference under varying wind speed and heat flux. *J. Phys. Oceanogr.,* **26,** 1969–1988.

Wu, X. Q., and W. L. Smith, 1997: Emissivity of rough sea surface for 8–13 μm: Modeling and verification. *Appl. Opt.,* **36,** 2609–2619.

Yamaguchi, Y., A. B. Kahle, H. Tsu, T. Kawakami, and M. Pniel, 1998: Overview of Advanced Spaceborne Thermal Emission Reflectance Radiometer. *IEEE Trans. Geosci. Remote Sens.,* **36,** 1062–1071.

Zavody, A. M., C. T. Mutlow, and D. T. Llewellyn-Jones, 1995: A radiative transfer model for SST retrieval for the ATSR. *J. Geophys. Res.,* **100,** 937–952.